metals

MDPI

Article

Comparative Study of Laser and GMAW Technologies: Effects on Mechanical Strength and Salt Spray Corrosion Performance of SGH340D + ZMA Galvanized Automotive Steel

Stefan Dikić [1,2,*], Hongqiang Liu [2,3], Dragomir Glišić [1,2], Jin Pan [2,3], Yongning Zhou [2,3], Nenad Radović [1,2] and Cheng Ma [2,3,*]

[1] Faculty of Technology and Metallurgy, University of Belgrade, 11000 Belgrade, Serbia; gile@tmf.bg.ac.rs (D.G.); nenrad@tmf.bg.ac.rs (N.R.)
[2] China-Serbia Belt and Road Joint Laboratory on Green Steel Manufacturing, Shijiazhuang 050023, China; panjin@hbisco.com (J.P.); zhouyongning@hbisco.com (Y.Z.)
[3] HBIS Materials Technology Research Institute, Shijiazhuang 050023, China
* Correspondence: sdikic@tmf.bg.ac.rs (S.D.); macheng01@hbisco.com or macf@mail.ustc.edu.cn (C.M.)

Abstract

The aim of this work is to investigate the influence of different welding technologies on the mechanical properties and corrosion resistance of welded joints of SGH340D + ZMA steel with a Zn–Mg–Al (ZMA) protective coating. Two different welding technologies were used: the gas metal arc welding(GMAW) process at a welding speed of 0.8 m/min and laser welding at speeds of 2 and 4 m/min. Mechanical properties were determined using tensile testing and hardness testing. Corrosion resistance was estimated using a salt spray test. Residual stresses were determined experimentally using the drill hole method. The highest residual stresses were measured in GMAW-welded joints, while the lowest were measured in laser-welded joints at a speed of 4 m/min. The sample welded by laser at a speed of 4 m/min exhibited hardness values close to the upper acceptable limit, indicating that further increases in welding speed without preheating may lead to excessive hardness. All samples exhibited good corrosion resistance in a salt chamber. According to the results, increased welding speed reduced residual stresses but increased the risk of brittle fracture.

Keywords: automotive industry; steel; SGH340D + ZMA; welding; laser; GMAW; corrosion resistance; salt spray test

Check for updates

Academic Editor: Dariusz Rozumek

Received: 2 June 2026
Revised: 24 July 2026
Accepted: 29 July 2026
Published: 12 August 2026

Copyright: © 2026 by the authors. Licensee MDPI, Basel, Switzerland. This article is an open access article distributed under the terms and conditions of the Creative Commons Attribution (CC BY) license.

1. Introduction

Due to increasingly rigorous environmental regulations, fuel-efficiency targets, cost reductions, and safety requirements, over the last decade, the automotive industry has undergone significant transformations. Consequently, there are significant and continuous efforts to reduce the weight of vehicles while preserving or enhancing structural integrity, safety, and durability. These constraints have imposed rigorous standards on steel materials, especially regarding high strength-to-weight ratio and corrosion resistance [1–5].

Despite the increased use of aluminum and polymer-based materials, steel remains the dominant structural material in the automotive industry, with a share of approximately 60% of the vehicle mass [1,2]. At the vehicle level, the effectiveness of lightweight material concepts is partially offset by the increasing integration of electrification systems, safety features, and comfort-related components. As a result, the average weight of a passenger vehicle has increased in recent years, particularly in the European market [2,5,6]. This trend

further emphasizes the significance of supporting complex steel production processes, including forming and welding, while reducing negative outcomes such as distortion or premature failure [7,8].

Although the use of advanced high-strength steel (AHSS) and ultra-high-strength steel (UHSS) has enabled significant weight reductions in selected safety-critical components, structural and HSLA steels continue to play a central role in automotive structures, especially in chassis systems, reinforcements, and welded assemblies designed for automated production. Their widespread use is primarily attributed to their cost efficiency, excellent formability and good weldability, which remain essential for high-volume manufacturing [3,4].

Besides mechanical performance, due to working conditions, which imply long exposure to a harsh environment, automotive steels must also comply with corrosion resistance requirements [9,10]. This requirement has driven the widespread adoption of coated steels, such as galvanized grades [10–14].

Equally important is the control of residual stresses, which may arise during forming and joining operations. Excessive residual stresses can negatively affect fatigue life, dimensional accuracy, and service performance, particularly in welded structures [7,8].

Given that modern automotive bodies and chassis systems consist of a large number of welded joints, the interactions between material properties, microstructural stability, and welding-induced thermal cycles become a critical aspect of structural integrity. HSLA steels with tailored compositions and controlled processing are therefore increasingly favored, as they enable reliable welding behavior and improved control of residual stresses, while still meeting lightweight design objectives [5,7].

Alongside efforts to reduce structural weight while ensuring safety on the roads, significant attention is also devoted to lowering production costs and improving manufacturing efficiency and effectiveness. Consequently, the use of galvanized steels is of great importance, as it eliminates the need for subsequent protection of entire structures against corrosion. At the same time, efforts are directed toward increasing welding speeds while maintaining adequate corrosion resistance and low levels of residual stresses.

Hot-dip zinc-coated structural steel sheets provide a favorable combination of moderate yield strength and high ductility, allowing efficient forming operations while ensuring sufficient load-bearing capacity [4–6].

Although this group of steels offers many advantages, galvanic coating poses a major challenge in welding due to porosity as a result of zinc evaporation during welding and related issues, such as sputtering and poor arc stability [15–19]. These problems are particularly pronounced when attempting to increase welding speed to increase productivity and reduce production costs.

Even though numerous studies have investigated laser and GMAW of galvanized automotive steels, most of them focused on either mechanical properties or corrosion resistance. Only limited attention has been devoted to the simultaneous evaluation of residual stresses, corrosion resistance, and mechanical performance under different welding technologies and welding speeds. Furthermore, comparative studies on SGH340D + ZMA steel remain scarce. Therefore, the aim of this work was to investigate the combined influence of heat input and welding speed on residual stresses, mechanical properties, and corrosion resistance of SGH340D + ZMA automotive steel, using two welding techniques for comparison: laser welding and GMAW. Such an integrated approach provides a more complete assessment of the suitability of these welding processes for high-productivity automotive manufacturing without compromising long-term structural integrity [7,8,20].

2. Materials and Methods

2.1. Materials

Hot-rolled grade SGH340D + ZMA steel sheets, 1.8 mm in thickness, were used in this study. The metallic coating (ZMA) was applied by a hot-dip galvanizing process on both surfaces of the sheets. The ZMA coating mass of 275 g/m^2 consists of zinc alloyed with magnesium and aluminum, which provides enhanced corrosion resistance compared to conventional zinc coatings. In addition, a thin anti-fingerprint finishing layer was applied as the outermost surface treatment.

Chemical composition of the tested steel alongside the standard requirements, and the chemical composition of the filler metal for the GMAW process are given in Table 1. All steel samples used for the investigation were obtained from the same batch. Mechanical properties of the investigated steel samples and filler metal, obtained from the corresponding material certificates provided by manufacturers, are given in Table 2.

Table 1. Chemical composition of SGH340D + ZMA steel (wt. %).

	C	Mn	Si	Al	Ti	V	P	S
JIS G3302 [21]	max. 0.25	max. 1.70	-	-	-	-	max. 0.20	max. 0.05
Tested steel	0.18	0.23	0.18	0.028	0.002	0.002	0.013	0.002
Filler metal	0.06–0.14	1.30–1.60	0.70–1.00	0.02	max. 0.15	max. 0.03	max. 0.025	max. 0.025

Table 2. Tensile properties of steel SGH340D + ZMA.

	Reh (MPa)	Rm (MPa)	A50 (%)
JIS G3302 [21]	min. 245	min. 340	min. 20
Tested steel	338	456	24
Filler metal in welded state	470	560	26

2.2. Welding

Steel plates of different sizes were cut from the steel sheets using precision cutting by Wire Electrical Discharge Machining (Wire EDM) (Sanguang HB400, Suzhou Sanguang Science & Technology Co., Ltd., Suzhou, China). The preparatory details of welding workpieces are illustrated in Figure 1. The gap between workpieces, X in Figure 1, was 0.05 mm for laser welding and 0.8 mm for GMAW.

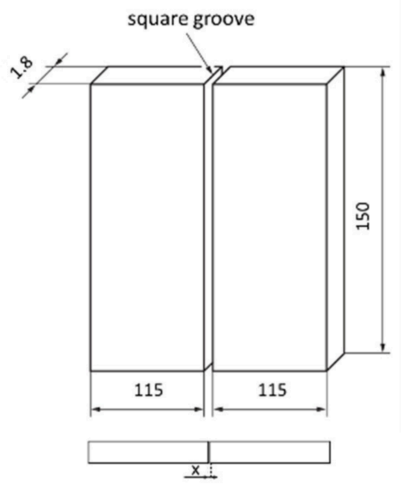


Figure 1. Dimensions (given in mm) of workpieces and groove preparation.

All the welded pieces were placed horizontally and fixed with a tool to enable single-pass welding in a flat position (PA).

The first set of workpieces was welded using the GMAW process, using a CMTwelding machine (CMT Advanced 4000R, Fronius, Austria), automated with the robotic system KR C4 smallsize-2. Two sets of workpieces were welded using an IPG Laser 12000-K fiber laser welding machine (IPG Photonics, Oxford, MA, US), equipped with a Fanuc Robot M-20iA25 (Beijing Fanuc Co, Ltd., Beijing, China). Welding parameters are shown in Table 3. The selected laser welding speeds were defined based on industrial requirements and with the aim of increasing productivity, while maintaining acceptable weld joint properties. The welding speed of 2 m/min was selected as commonly used in industrial practice, whereas the welding speed of 4 m/min was selected for an increased productivity condition. Higher welding speeds render hardness values at the upper acceptable limit. Therefore, a further increase would lead to excessive hardness due to higher cooling rates.

Table 3. Welding parameters.

	Current [A]	Voltage [V]	Power [kW]	Welding Speed [m/min]	Wire Feed [m/min]	Protective Gas	Gas Flow [L/min]	Heat Input [J/mm]	Off Focus [mm]
GMAW	134	17	-	0.8	3.2	80%Ar + 20%CO_2	15	138	-
Laser	-	-	3.5	2	-	100%Ar	20	74	14
	-	-	5.6	4	-	100%Ar	20	59	14

2.3. Visual Testing

Prior to performing mechanical, microstructural, and corrosion tests, all samples were visually tested (VT) in accordance with the appropriate standard [22]. Only samples that passed the VT were subjected to further testing.

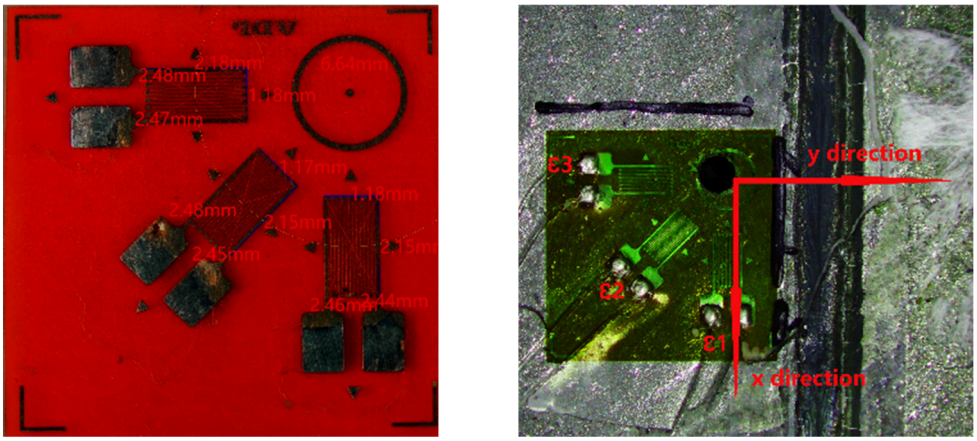
2.4. Residual Stress Testing

Residual stress measurements were carried out using the hole-drilling method in accordance with the relevant international standard ASTM E837—Standard Test Method for Determining Residual Stresses by the Hole-Drilling Strain-Gage Method [23]. The measurements were performed by drilling a through hole with a 1.5 mm diameter drill bit. Two samples of base metal and two for each welding technology were tested. Strain relief resulting from material removal during drilling was monitored using Type B strain gauge ASTM E837 rosettes (three gauges placed at a 45° angle to each other) as shown in Figure 2a. The rosette was positioned next to the weld metal, aiming at the heat-affected zone (HAZ), as shown in Figure 2b. The measured strain relaxation was used as an indicator of the residual stress state in the welded sheets. Before positioning the rosette, the surface was properly cleaned and prepared for testing. The method was employed to qualitatively assess differences in residual stress levels induced by different welding processes. Average values of geometric parameters of rosette positioning is shown in Table 4.

Table 4. Average values of geometric parameters of rosette positioning.

	Hole Center to Weld Edge (mm)	Hole Center to Weld Center Line (mm)	Hole Diameter (mm)	Angle Between Weld Direction and X Direction
Laser 2 m/min	3.23	4.3	1.5	0.71°
Laser 4 m/min	3.2	4.32	1.5	-
GMAW	3.67	4.38	1.5	2.36°

The accuracy of the measuring device was ±0.016 mm, as specified in the calibration certificate.



(**a**) (**b**)

Figure 2. Setup for residual test: (**a**) rosette Type B and (**b**) position of drill hole.

2.5. Mechanical Testing

Tensile test specimens, two from each joint, were sampled in accordance with the recommendation of the standard [24]. The tensile testing technique was performed at ambient temperature, in accordance with the EN ISO 4136 [25] and EN ISO 6892-1 [26] requirements concerning Method A as the testing method. The engineering strain rate was controlled at 0.00025 s^{-1} up to the onset of yielding, after which it was increased to 0.0067 s^{-1} and maintained until fracture. Therefore, the testing parameters were not considered as experimental variables in this study. The geometry and dimensions of the tensile specimens are presented in the schematic drawing in Figure 3 and were in accordance with the EN ISO 4136 standard. The specimen dimensions were verified using a measuring device with an accuracy of ±0.016 mm, which is significantly lower than the dimensional tolerance permitted by the applied standard. The test was conducted using a tensile testing apparatus, ZWICK ROELL Z100THW (ZwickRoell Testing Technology Co., Ltd., Ulm, Germany), and equipped with extensometer BT2-EXMACRO.H12 (ZwickRoell Testing Technology Co., Ltd., Ulm, Germany).

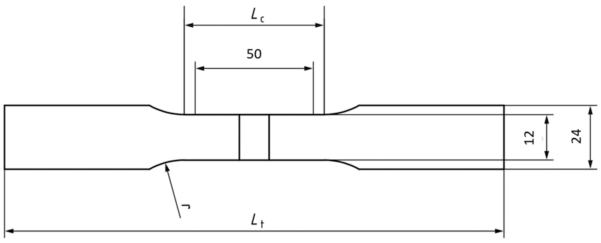


Figure 3. Geometry of tensile test specimen (in mm) according to EN ISO 4136.

Hardness measurements were performed on transverse cross-sections of the welded joints using the Vickers hardness method (HV0.2) in accordance with EN ISO 9015-2 [27] and EN ISO 6507-1 [28]. The measurements were conducted along a single measurement line positioned at the mid-thickness of the joint cross-section, covering the base material, heat-affected zone, and weld metal as illustrated in Figure 4. The distance between the centers of adjacent indentations was maintained at 0.2 mm, in compliance with the spacing requirements specified in the relevant standards. Hardness testing was conducted using a Wilson Hardness Tukon 2500 Minuteman hardness tester (Wilson Instruments, Norwood, MA, USA).

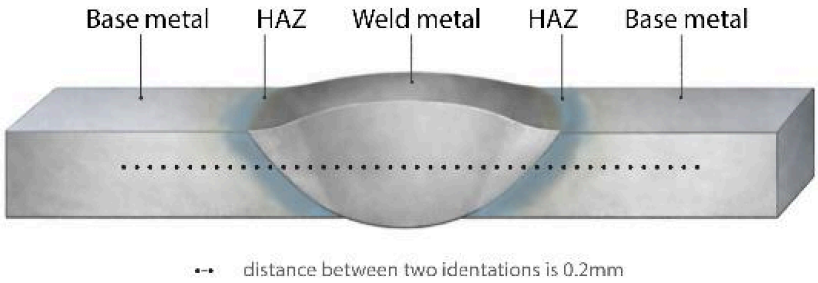


Figure 4. Illustration of position of hardness measuring line.

2.6. Metallographic Analysis

Metallographic samples were cut by Wire EDM in order to preserve the ZMA coating layer and to prevent excessive heat input. Samples were mounted in bakelite using a hot process and were mechanically prepared by grinding on wet sandpapers with different granulations up to P1000, followed by polishing with a 2.5 µm diamond powder polishing solution. Polished samples were chemically etched by a 2.5% solution of Nitric acid in Ethanol (Nital). Microstructural analysis was performed using a light microscope Zeiss Axio Imager.M2m equipped with a digital camera AxioCam MRc 5 (Carl Zeiss Microscopy GmbH, Jena, Germany) and software for image acquisition.

2.7. Salt Spray Test

Salt spray corrosion testing was conducted with a YWX/Q-020 salt spray chamber (Yangzhou Gaoke Testing Equipments, Yangzhou, China), adhering to established salt fog testing protocols. Testing sample dimensions were 100 × 150 mm, in accordance with standard EN ISO 9227 [29]. Distilled water with a resistivity exceeding 5 MΩ·cm at 25 ± 2 °C was used to prepare a 5% sodium chloride (NaCl) solution. Test specimens were mounted on a non-metallic stand in the chamber, so that more than 98% of their surface area was exposed to the salt fog. The chamber temperature was set to 45 °C, while the saturated air barrel temperature was maintained at 45–48 °C. Salt fog was generated continuously, providing a deposition rate of 1.35–1.50 mL h^{-1} per 80 cm^2 area. The test duration was 720 h or until the first traces of rust appeared at the sample surface.

3. Results

3.1. Visual Examination

Most of the joints were free of defects such as cracks, porosity, misalignment, undercuts, spattering, etc. (Figures 5 and 6). Some of the samples were excluded from further testing due to unacceptable defects such as misalignment.

Significant distortion was observed on the samples welded by the GMAW process. As can be seen from Figure 5, longitudinal distortion of GMAW-welded samples is very pronounced (Figure 5a,b) compared to the laser-welded samples (Figure 5c–f). Deformation is most easily observed at the corners of the specimens that are raised, as well as on the longer sides where the residual stresses caused buckling.

Metallographic samples of welded joints were used for macrostructural examination, as shown in Figure 6. Full penetration was achieved by each of the applied welding technologies. All of the geometric parameters of the joints are in accordance with EN ISO 5817 [30] for B quality of welded joints.

As can be seen from Figures 5 and 6, the width of the upper side of the weld metal obtained by GMAW is significantly greater than the values obtained on laser-welded samples. The width of the welded metal on the bottom side of the samples is significantly

bigger in laser-welded joints (Figure 6). The width of the HAZ in the GMAW samples is the largest, while the laser-welded joints (4 m/min) were narrower (Figure 6).

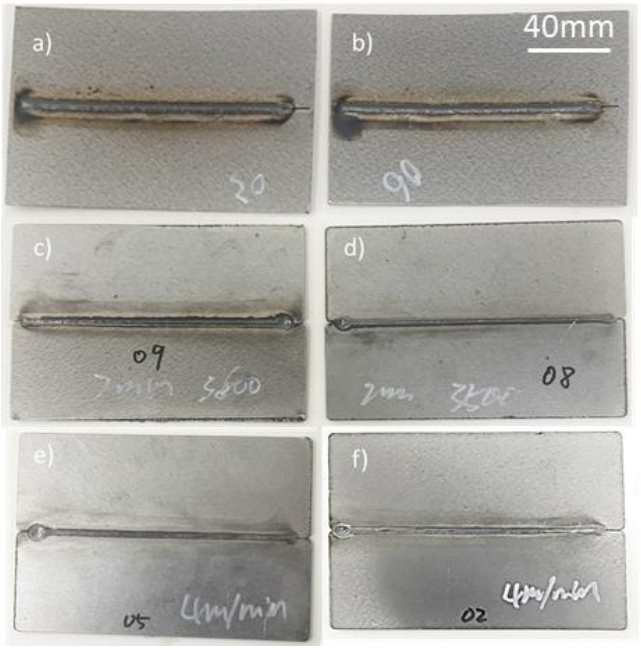
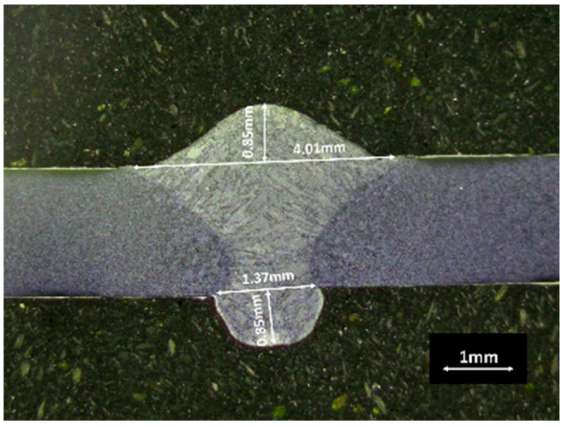
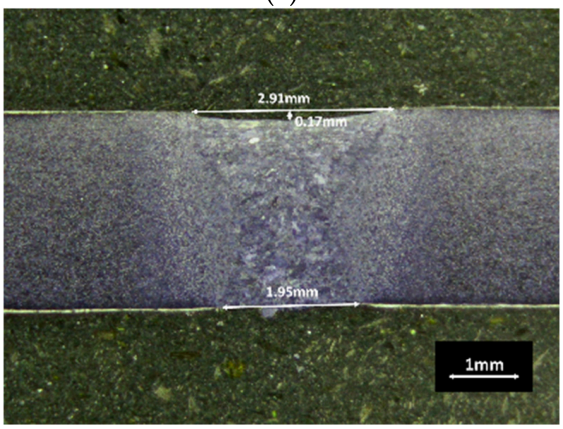


Figure 5. Appearance of welded joints: (**a**,**b**) GMAW; (**c**,**d**) laser welding speed 2 m/min; (**e**,**f**) laser welding speed 4 m/min.

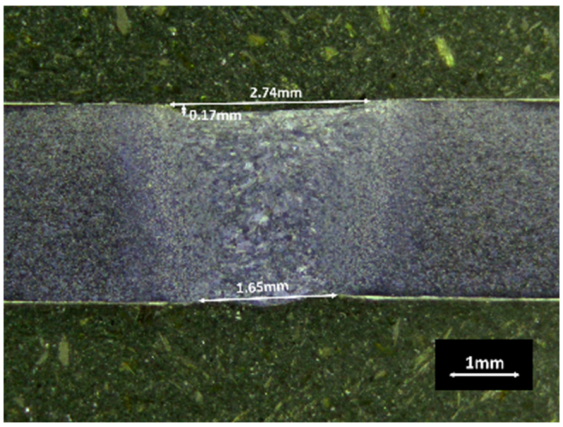


(**a**)



(**b**)

Figure 6. *Cont.*



(**c**)

Figure 6. Macro-analysis of welded joints: (**a**) GMAW, (**b**) laser 2 m/min, (**c**) laser 4 m/min.

3.2. Residual Stress

As shown in Figure 2b, the longitudinal direction of the welded joint was adopted as the X direction. The results, given in Table 5, indicate the highest residual stress values in the longitudinal direction, while the lowest were obtained in the Y direction. Residual stresses in the base metal are very low. However, after the welding, a significant increase in residual stress values is observed (Table 5). The highest stress was detected after GMAW, while the lowest was detected in laser-welded samples with a welding speed of 4 m/min.

Table 5. Residual stress measurements.

	σ_x	σ_y	τ_{xy}	σ_{max}	σ_{min}
Base metal	32.4 ± 1.2	22.9 ± 0.8	25.2 ± 0.5	53.3 ± 1.4	1.97 ± 0.2
Laser weld joint, 2 m/min	195.8 ± 3.6	−10.3 ± 1.1	−30.0 ± 0.8	200.1 ± 4.8	−14.55 ± 1.2
Laser weld joint, 4 m/min	123.7 ± 2.6	−17.8 ± 0.7	−37.6 ± 1.2	133.07 ± 3.2	−27.17 ± 0.7
GMAW joint	284.8 ± 4.6	90.0 ± 2.4	−172.2 ± 3.3	385.3 ± 4.8	−10.4 ± 0.8

σ_x and σ_y—residual normal stress components in the X (longitudinal) and Y (transverse) directions, respectively; τ_{xy}—in-plane shear (tangential) residual stress component; σ_{max} and σ_{min}—the maximum and minimum principal residual stresses, respectively.

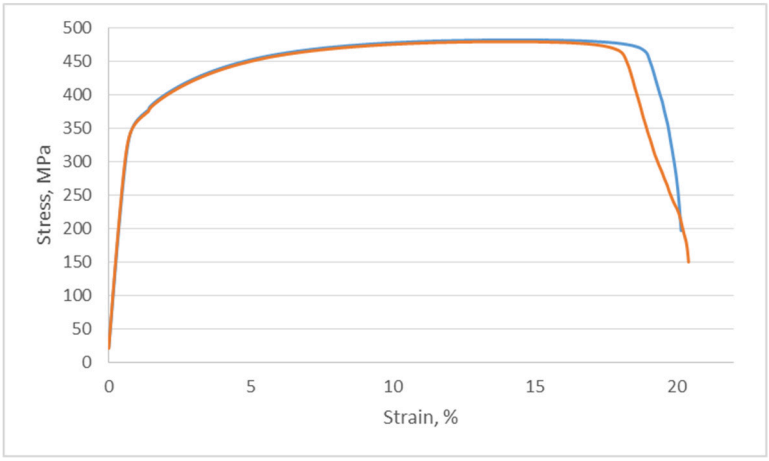
3.3. Tensile Testing

Stress–strain curves obtained by tensile testing of the welded joints are shown in Figure 7. The two curves in different colors correspond to the two specimens tested under the same welded joint and testing condition. The values of yield strength, ultimate tensile strength, and total elongation are given in Table 6.

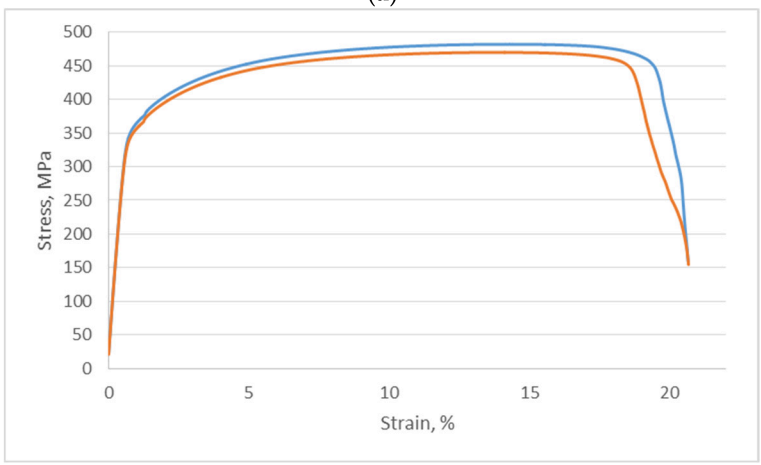
Table 6. Tensile properties of welded joints.

	$R_{p0.2}$, MPa	R_m, MPa	$A_{50,manual}$, %
GMAW	358 ± 0.5	480 ± 2	20.3 ± 0.3
Laser 2 m/min	352 ± 6	476 ± 8	20.8 ± 0.1
Laser 4 m/min	338 ± 1	454 ± 7	20.2 ± 0.7

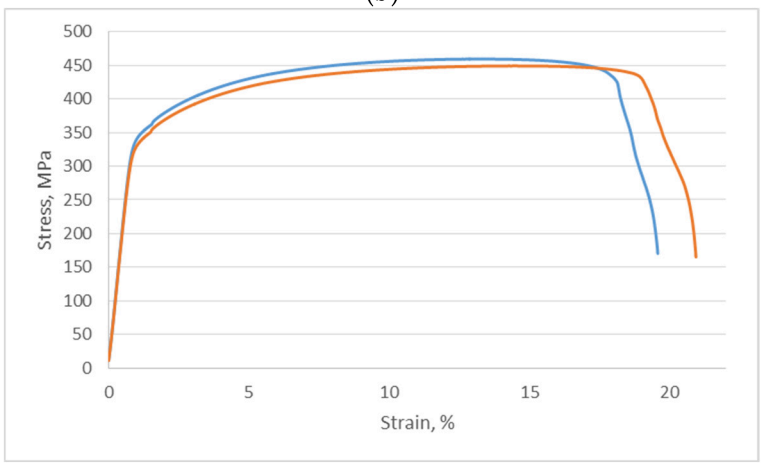
$R_{p0.2}$—yield strength; R_m—ultimate tensile strength; $A_{50,manual}$—manually determined total elongation based on the initial gauge length of 50 mm.



(**a**)



(**b**)



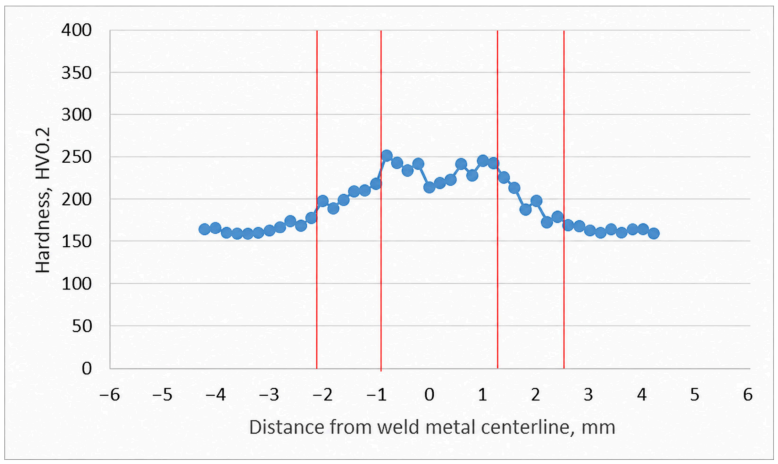
(**c**)

Figure 7. Stress–strain diagrams for different welding procedures: (**a**) GMAW, (**b**) laser 2 m/min, (**c**) laser 4 m/min.

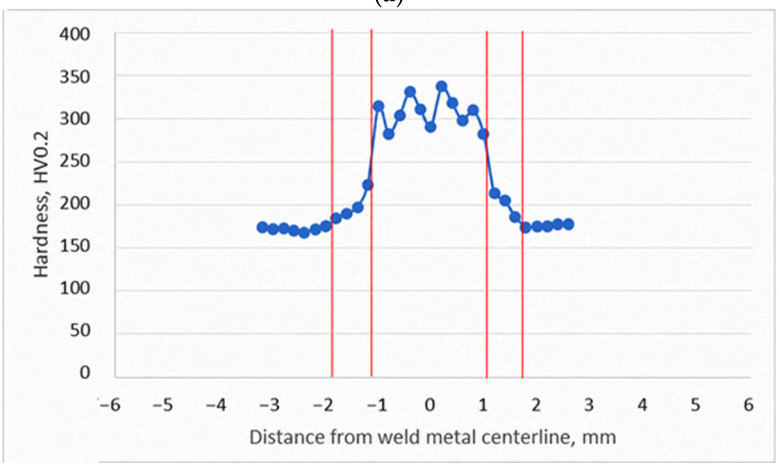
3.4. Hardness Testing

The distribution of hardness values along the line at the cross-section of the welded joint is shown in Figure 8. The hardness profile represents the spatial variation in hardness across the welded joint; therefore, each plotted value corresponds to a single measurement location. The highest values of hardness were exhibited in the weld metal of the laser-welded sample at a speed of 4 m/min, while the lowest hardness values in the weld metal

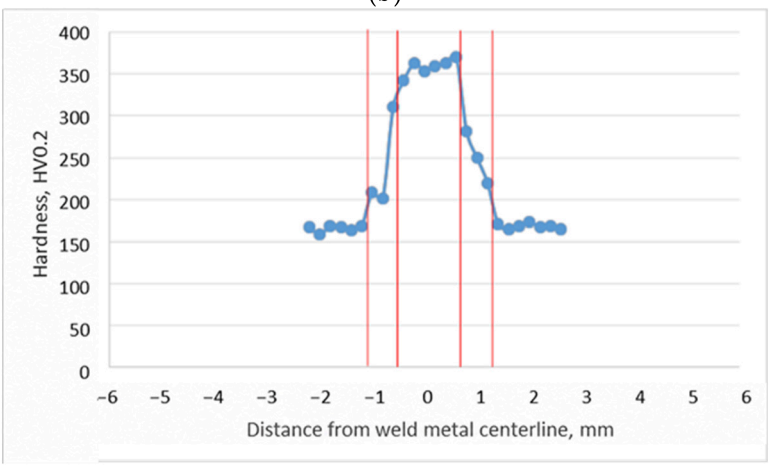
were measured in the GMAW-welded sample. According to the calibration certificate, the measurement error might be up to ±2.7%.



(**a**)



(**b**)



(**c**)

Figure 8. Distribution of hardness values through the welded joint: (**a**) GMAW, (**b**) laser 2 m/min, (**c**) laser 4 m/min.

3.5. Microstructural Analysis

The microstructure of the base metal, shown in micrographs in Figure 9, is homogeneous and consists of fine-grained ferrite and bainite with a small amount of pearlite.

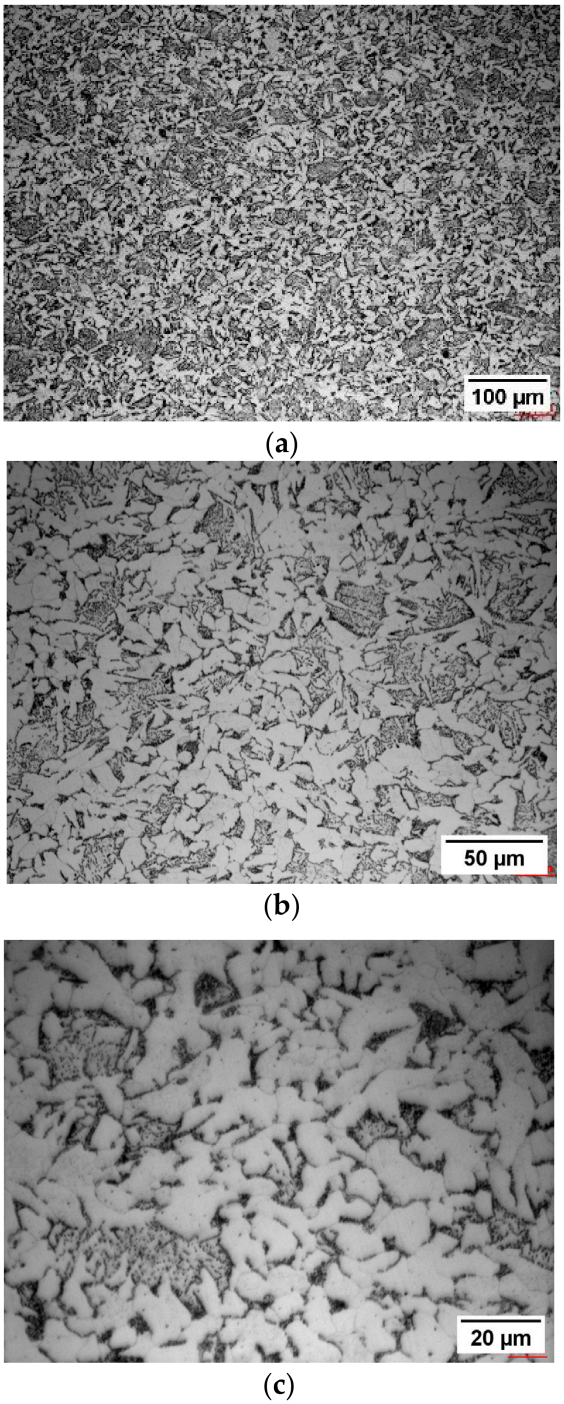


Figure 9. Representative micrographs of the base metal at different magnifications: (**a**) 100×, (**b**) 200×, and (**c**) 500×.

The microstructure of the HAZ of the GMAW-welded samples, shown in Figure 10a,b, is characterized as heterogeneous, consisting of coarse grain boundary ferrite (GBF), Widmanstätten ferrite (WF), bainite, and pearlite. In contrast, laser-welded samples produced at a welding speed of 2 m/min exhibit a significantly narrower HAZ (Figure 10c,d), with a ferritic–bainitic/pearlitic microstructure that is considerably finer compared to that observed in GMAW joints. Furthermore, in the laser-welded sample produced at a higher welding speed, 4 m/min, the microstructure within the HAZ region is predominantly bainitic, with only a minor presence of ferrites (predominantly GBF), as shown in Figure 10e,f.

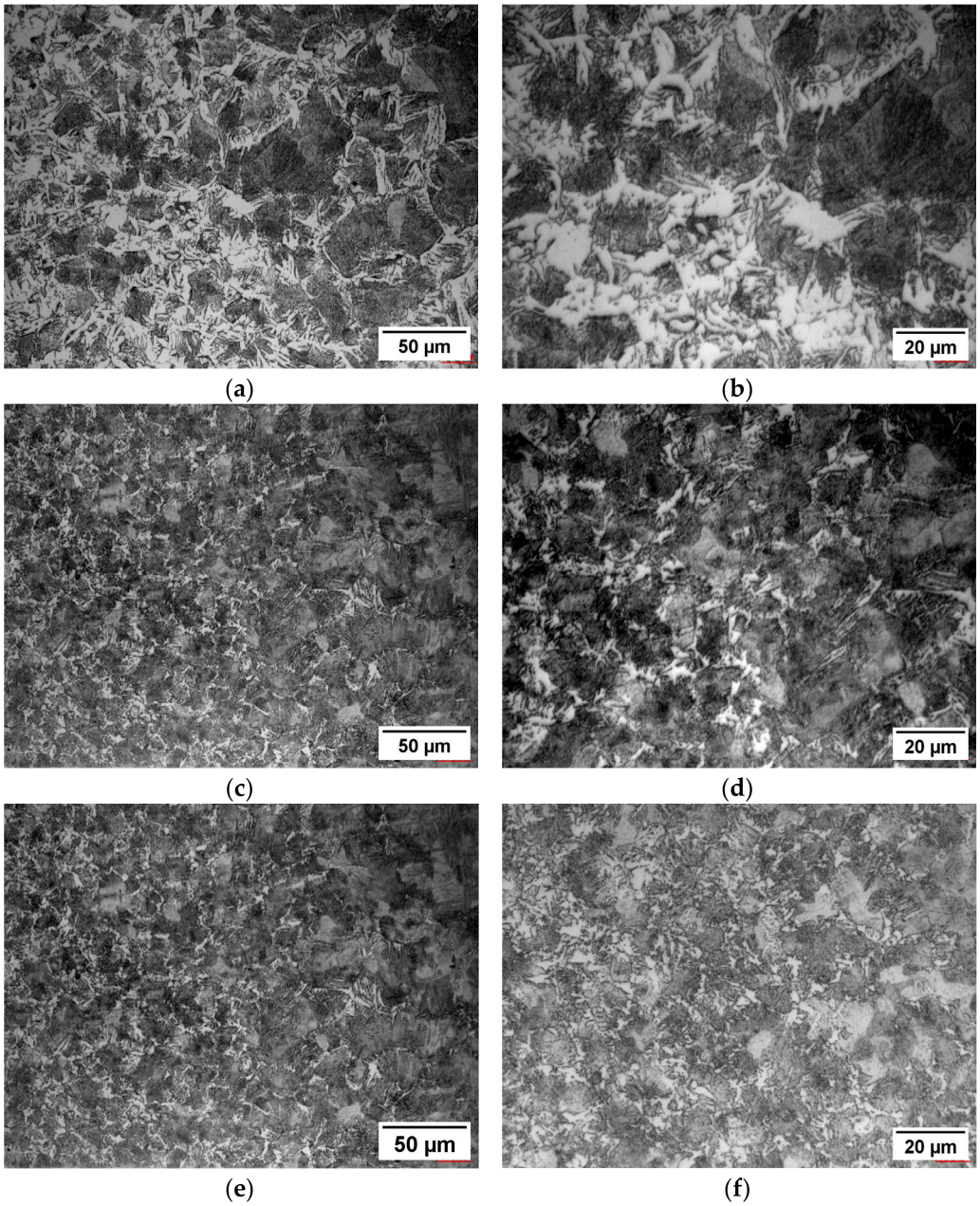


Figure 10. The microstructure of the heat-affected zone (HAZ): (**a**,**b**) GMAW-welded joint, (**c**,**d**) laser-welded joint at a welding speed of 2 m/min, and (**e**,**f**) laser-welded joint at a welding speed of 4 m/min. The micrographs were obtained at magnifications of 200× (**a**,**c**,**e**) and 500× (**b**,**d**,**f**).

The microstructure of the weld metal (Figure 11) in the GMAW sample consists of Widmanstatten ferrite, acicular ferrite (AF), and a small amount of bainite, while the microstructure of WM in laser-welded samples predominantly consists of martensite and bainite with GBF. Samples welded with a speed of 2 m/min are characterized by higher ferrite content, consisting of grain boundary allotriomorphs and WF, while samples welded at 4 m/min welding speed have lower ferrite content, predominantly WF.

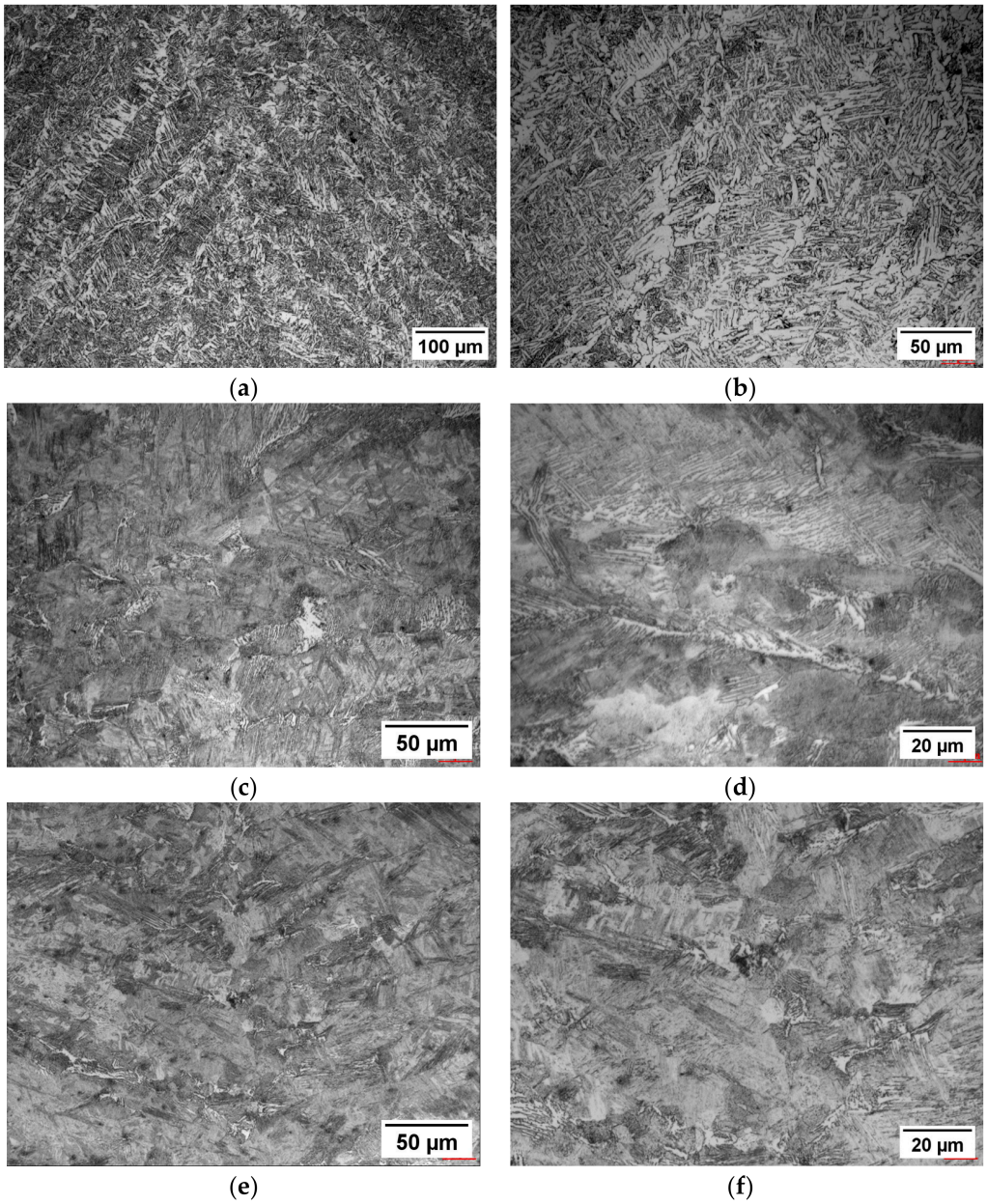


Figure 11. The microstructure of the weld metal (WM): (**a**,**b**) GMAW-welded joint, (**c**,**d**) laser-welded joint at a welding speed of 2 m/min, and (**e**,**f**) laser-welded joint at a welding speed of 4 m/min. The micrographs were obtained at magnifications of 200× (**a**,**c**,**e**) and 500× (**b**,**d**,**f**).

3.6. Anti-Corrosion Test

Samples subjected to the salt spray test were checked every week for the occurrence of rust on the surface. During the test, all specimens were positioned in the salt spray chamber in the same orientation, as shown in Figure 12. Therefore, the photographs presented after the exposure correspond to the actual orientation of the specimens during the corrosion test. Figure 12 presents the surface appearance of the samples before exposure, after 360 h, and at the end of the salt spray test (after 720 h). Specifically, Figure 12a–c show the surfaces of samples laser welded at a speed of 4 m/min, Figure 11d–f correspond to samples welded at 2 m/min, and Figure 12g–i illustrate the GMAW samples.

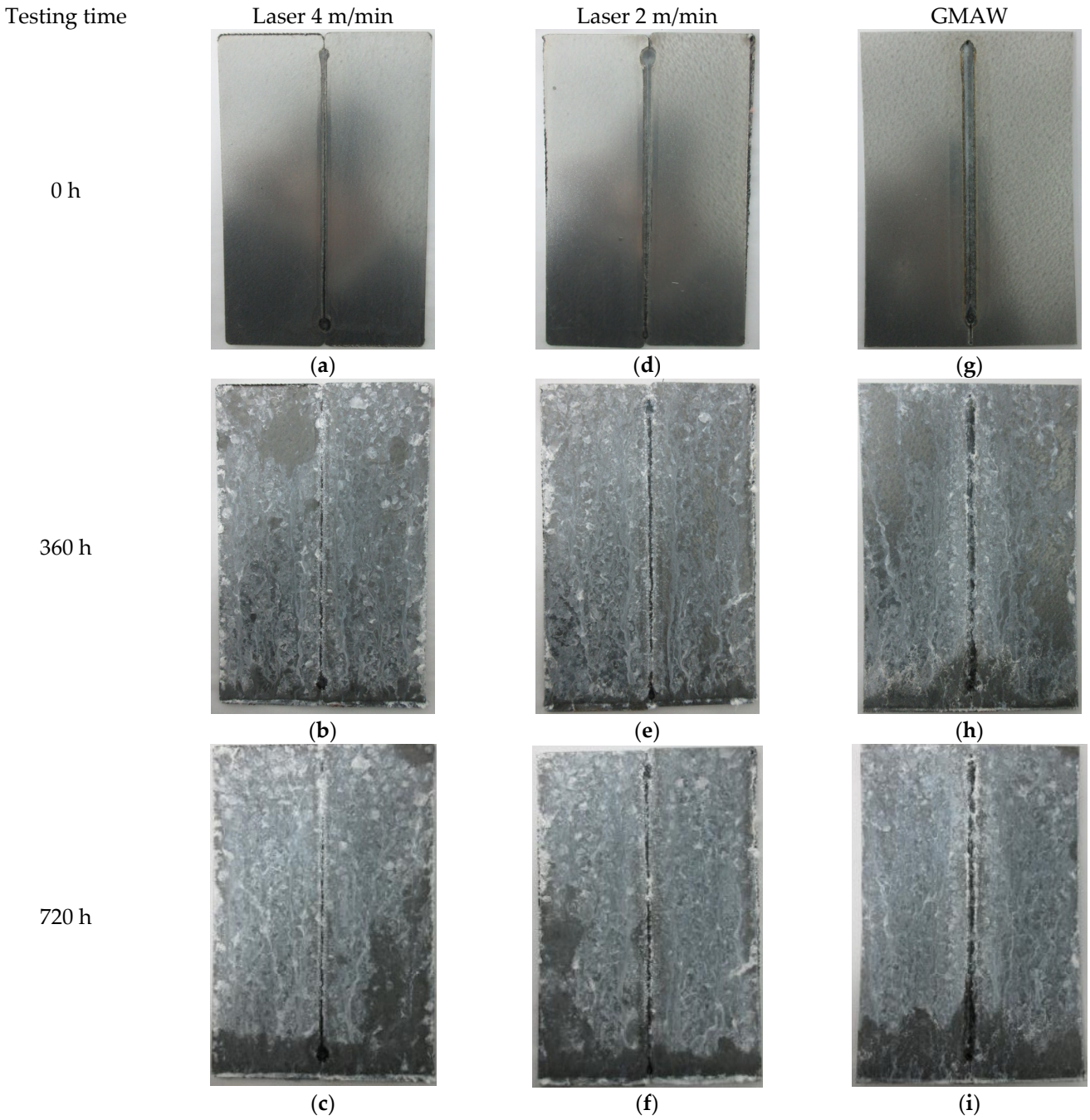


Figure 12. Sample surfaces: (**a**–**c**) before the salt spray; (**d**–**f**) after 360 h; (**g**–**i**) after 720 h.

No white corrosion products were observed on the specimen surfaces prior to exposure. The formation of white corrosion products was detected only after the samples were subjected to the salt spray test, with no evidence of red rust throughout the testing period. After 360 h of exposure, nearly the entire weld metal of the laser-welded joint produced at 4 m/min was covered with white corrosion products, whereas the GMAW sample exhibited the lowest degree of surface coverage.

After 720 h, the weld metal of the laser-welded samples was almost completely covered with white corrosion products. In contrast, although a significant portion of the GMAW sample surface was affected, complete coverage was not observed.

4. Discussion

The heat input of the GMAW process, at 138 J/mm, markedly exceeded the heat input achieved using the laser welding processes (Table 3). Such a high thermal input caused the formation of a wide molten pool and a wide heat-affected zone (HAZ), which in turn caused pronounced strains, as a consequence of the shrinkage of the welded specimens [7,8,31–35]. Consequently, the GMAW-welded joint exhibited the highest residual stress levels, with a maximum principal stress of $\sigma_{max} \approx 385$ MPa, which significantly exceeded the yield strength of the SGH340D steel. Such high residual stresses are consistent with the observed macroscopic distortions of the thin sheets, as shown in Figure 5a,b.

In contrast, the lower heat input of the laser welding process, 74 J/mm and 59 J/mm for welding speeds of 2 m/min and 4 m/min, respectively, and the concentrated energy density characteristic of the laser source resulted in narrower weld metal and a narrower HAZ [31–33]. This is reflected in the lower residual stress magnitudes measured in the laser-welded joints. Increasing the welding speed from 2 to 4 m/min further reduced the maximum principal stress from approximately 200 MPa to 133 MPa, confirming the strong inverse relationship between the heat input and residual stress magnitude [31,32,36]. In particular, the residual stresses in the samples obtained by laser welding at a speed of 4 m/min are approximately two to almost three times lower than in the case of GMAW-welded specimens. Furthermore, residual stresses of the laser-welded samples were lower than the yield strength of the base metal; therefore, no significant deformations were observed, as shown in Figure 5c–f. These findings are consistent with previously reported studies on welding-induced residual stresses and distortion control in thin-gauge steel structures [31,32].

For each investigated welding condition and for the base metal, two tensile specimens were tested. The obtained stress–strain curves showed nearly complete overlap for all conditions (Figure 7), indicating high reproducibility and stable mechanical properties, and confirming that testing a larger number of specimens was not necessary.

The obtained values of yield strength ($R_{p0.2}$) and ultimate tensile strength (Rm) showed only minor variations between samples for different welding processes. The yield strength ranged from 338 MPa to 358 MPa, while the ultimate tensile strength varied between 454 MPa and 480 MPa. Similarly, the total elongation remained very consistent for all specimens, with values between 20.2% and 20.8%. The elongation of the welded specimens was slightly lower than that of the base metal (24%). This reduction can be attributed to microstructural heterogeneities and locally increased strength in the weld region. The higher strength of the heat-affected zone and weld metal, resulting from phase transformations, and the influence of the filler material in GMAW (Table 2) further contribute to reduced uniform plastic deformation during tensile loading [37,38]. When compared to the requirements specified in the JIS G3302 standard, which defines minimum values of 245 MPa for yield strength, 340 MPa for tensile strength, and 20% for elongation, all tested conditions are well within the expected range for SGH340D steel and demonstrate sufficient strength and ductility.

The hardness distributions across the welded joints clearly reflect the combined influence of welding heat input, cooling rate, and the resulting microstructural evolution in SGF340D steel. The GMAW joint, characterized by the highest heat input and the lowest cooling rate, respectively, exhibits a relatively smooth hardness gradient from the base metal towards the weld metal, accompanied by a wide heat-affected zone [19,39–42]. The moderate increase in hardness values observed in the HAZ and WM region is consistent with the formation of WF, AF, and a limited fraction of bainite (Figure 11) [17,18,39,41–44]. Microstructural constituents observed in GMAW-welded samples (Figure 11a,b) are typically associated with intermediate cooling rates, particularly in the case of acicular ferrite

and bainite, where phase transformations proceed through a combination of diffusional and displacive mechanisms. Increased hardness values might be explained by higher bainite content compared to the base metal, but also different ferrite morphologies that are characterized by higher dislocation density [45]. In contrast, the laser-welded joints demonstrate markedly different hardness values in HAZ and WM, primarily governed by the significantly reduced heat input and thermal cycles, which include higher cooling rates. For the laser welding speed of 2 m/min, the narrower HAZ and the steep hardness gradients indicate accelerated cooling, leading to the formation of a finer ferritic–bainitic microstructure in the HAZ and a weld metal predominantly composed of martensite and bainite with grain boundary ferrites [17,18]. The increased hardness level in the weld metal compared to the GMAW joint can therefore be attributed to the higher share of displacive transformation mechanism and microstructure refinement. Further increasing the welding speed to 4 m/min results in the lowest heat input and the highest cooling rate, which strongly promote martensitic and bainitic transformations in the weld metal while suppressing ferrite formation to a very small portion of the microstructure. Consequently, the highest peak hardness values are recorded in this joint, along with an extremely narrow HAZ and abrupt transitions toward the base metal hardness. While the acquired hardness values (below 380 HV, the upper hardness limit established by the standard [24]) are advantageous for joint strength and minimal thermal degradation of adjacent material, the significant hardness gradients may also suggest a heightened vulnerability to brittle behavior, consequently restricting further enhancements in welding speed without preheating.

The corrosion behavior of the welded samples subjected to salt spray testing demonstrates a high level of surface protection provided by the Zn–Mg–Al (ZMA) coating. After 360 h of exposure, only white corrosion products were observed on the specimen surfaces, while no red rust associated with degradation of the steel substrate was detected. The reduced heat input in laser welding, resulting in a narrower weld metal zone, leads to a greater portion of the joint surface exhibiting white corrosion compared to Gas Metal Arc Welding (GMAW). This behavior is primarily related to the response of the ZMA coating, which undergoes partial melting and non-uniform redistribution under rapid thermal cycles, causing local discontinuities and electrochemical heterogeneity [12,46,47]. Additionally, the multiphase nature of the coating and limited chemical composition homogenization promotes micro-galvanic effects, increasing susceptibility to localized corrosion, particularly in the fusion zone [48]. In contrast, the higher heat input in GMAW enables more uniform coating redistribution, reducing compositional gradients and consequently the extent of white corrosion [12,47]. The formation of white corrosion products is a typical feature of ZMA-coated steels and has been widely reported in the literature [12,47]. Based on previous work by Volovitch et al. [47] and Malla et al. [49], it is assumed that these products predominantly consist of zinc hydroxides and oxides, as well as complex Zn–Mg–Al hydroxide and hydroxychloride phases formed during the initial stages of exposure to chloride-containing environments [47,49]. In this case, the formation of white corrosion on the ZMA coating has a predominantly protective role rather than being detrimental. In addition, the coating provides sacrificial protection, as zinc preferentially corrodes instead of the steel substrate, effectively delaying the onset of red rust even in regions with local coating damage or heterogeneity. This effect is particularly important in welded joints, where microstructural and compositional variations can promote localized electrochemical activity [47,49].

The absence of traces of red corrosion on the surface of the samples after 720 h indicates that, regardless of the inevitable degradation of the surface protective ZMA layer due to welding, its protective function had not degraded significantly. Due to the higher heat input and larger weld width of the GMAW joint, it takes more time to create a layer of white

corrosion on the weld surface and HAZ, which may indicate that the GMAW joints are more vulnerable and prone to the occurrence of red corrosion. This finding is particularly relevant for automotive sheet steels, where welded joints are often considered critical locations for accelerated corrosion due to localized thermal damage of protective coatings [39]. The present results suggest that, especially in the case of low-heat-input laser welding, the protective functionality of the ZMA coating is largely preserved, ensuring adequate corrosion resistance of the welded joints under aggressive environmental conditions.

5. Conclusions

- By changing the welding process from GMAW to laser and increasing the speed of the laser welding, a significant reduction in heat input and residual stresses was achieved. While the GMAW joint showed a complex multiaxial stress state, prone to distortion and buckling, the laser-welded joints remained largely dimensionally stable, in agreement with experimental observations.
- The excellent agreement between duplicate tensile tests, the narrow range of mechanical property variations, and compliance with standard requirements confirm that the applied welding technologies did not affect the strength of the steel, making it suitable for automotive structural applications.
- Both GMAW and laser welding procedures provided welded joints with acceptable hardness values according to relevant standards [24]. While the GMAW-welded joints exhibit somewhat lower hardness and more gradual hardness distribution, laser-welded joints exhibit narrower, high-hardness joints due to rapid cooling and the formation of a predominantly martensite/bainite microstructure.
- More concentrated energy of the laser beam creates a narrower weld and a lower degradation level of the protective layer compared to the GMAW process. In this way, degradation of the protective surface ZMA layer was reduced, and occurrence of white corrosion across the HAZ and WM of laser-welded samples was also reduced compared to GMAW. Resistance to red rust, which could potentially significantly compromise the integrity of the joints, was maintained even after very long periods of continuous exposure to an aggressive environment in the salt spray test.

Author Contributions: Conceptualization, S.D., C.M. and D.G.; methodology, N.R., Y.Z. and H.L.; validation, S.D., C.M. and J.P.; formal analysis, J.P.; investigation, S.D.; resources, H.L.; data curation, D.G., Y.Z. and J.P.; writing—original draft preparation, S.D.; writing—review and editing, C.M., D.G., N.R. and H.L.; visualization, J.P. and Y.Z.; supervision, H.L. and N.R. All authors have read and agreed to the published version of the manuscript.

Funding: The research is funded by China's key R&D program project titled China-Serbia Belt and Road joint laboratory construction and joint research project for green steel manufacturing (No. 2024YFE0215000). This work was financially supported by the Ministry of Science, Technological Development and Innovation of the Republic of Serbia (Contract No. 451-03-34/2026-03/200135).

Data Availability Statement: The original contributions presented in this study are included in the article. Further inquiries can be directed to the corresponding authors.

Acknowledgments: The authors acknowledge that the results presented in this study originated from Dikić Stefan's participation in the Talented Young Scientist Program.

Conflicts of Interest: Liu Hongqiang, Pan Jin, Yongning Zhou, and Ma Cheng were employed by the HBIS Materials Technology Research Institute, Shijiazhuang, Hebei, 050023. The remaining authors declare that the research was conducted in the absence of any commercial or financial relationships that could be construed as a potential conflict of interest.

References

1. WorldAutoSteel. *Future Steel Vehicle (FSV): Lightweighting Potential of Advanced High-Strength Steels*; WorldAutoSteel: Brussels, Belgium, 2024. Available online: https://www.worldautosteel.org (accessed on 5 January 2026).
2. International Council on Clean Transportation (ICCT). *Green Steel Supply: Implications for the Automotive Industry*; ICCT: Washington, DC, USA, 2024. Available online: https://theicct.org (accessed on 5 January 2026).
3. Kuziak, R.; Kawalla, R.; Waengler, S. Advanced High Strength Steels for Automotive Industry. *Arch. Civ. Mech. Eng.* **2008**, *8*, 103–117. [CrossRef]
4. Matlock, D.K.; John, G. Speer Third Generation of AHSS: Microstructure Design Concepts. In *Microstructure and Texture in Steels: And Other Materials*; Springer: London, UK, 2009; pp. 185–205.
5. Tisza, M. Development of Lightweight Steels for Automotive Applications. In *Engineering Steels and High Entropy-Alloys*; IntechOpen: London, UK, 2020.
6. Davies, G. *Materials for Automotive Bodies*; Elsevier: Amsterdam, The Netherlands, 2012.
7. Totten, G.E. *Handbook of Residual Stress and Deformation of Steel*; ASM International: Almere, The Netherlands, 2002.
8. Withers, P.J.; Bhadeshia, H.K.D.H. Residual Stress Part 1-Measurement Techniques. *Mater. Sci. Technol.* **2001**, *17*, 355–365. [CrossRef]
9. Almeraya-Calderón, F.; Montoya-Rangel, M.; Nieves-Mendoza, D.; Jáquez-Muñoz, J.M.; Diaz-Olivares, A.; Lara-Banda, M.; Maldonado-Bandala, E.; Estupian-Lopez, F.; Cabral-Miramontes, J.; Olguin-Coca, J.; et al. Corrosion Behavior of Advanced High-Strength Steels (AHSS) in Chloride Solutions for Automotive Applications. *Metals* **2025**, *15*, 1116. [CrossRef]
10. Roberge, P.R. *Handbook of Corrosion Engineering*; McGraw-Hill Education: Columbus, OH, USA, 2019.
11. Raja, P.B.; Ismail, M.; Ghoreishiamiri, S.; Mirza, J.; Ismail, M.C.; Kakooei, S.; Rahim, A.A. Reviews on Corrosion Inhibitors: A Short View. *Chem. Eng. Commun.* **2016**, *203*, 1145–1156. [CrossRef]
12. Guo, T.; Wang, Y.; Yu, L.; Jin, Y.; Zeng, B.; Dou, B.; Liu, X.; Lin, X. Roles of Al and Mg on the Microstructure and Corrosion Resistance of Zn-Al-Mg Hot-Dipped Coated Steel. *Materials* **2024**, *17*, 1512. [CrossRef] [PubMed]
13. Marcus, P. On some fundamental factors in the effect of alloying elements on passivation of alloys. *Corros. Sci.* **1994**, *36*, 2155–2158. [CrossRef]
14. Marcus, P.; Protopopoff, É.; Maurice, V. Surface Chemistry and Passivation of Metals and Alloys. In *Mechanics-Micro-Structure-Corrosion Coupling: Concepts, Experiments, Modeling and Cases*; Elsevier: Amsterdam, The Netherlands, 2019; pp. 91–120.
15. Tasalloti, H.; Kah, P.; Martikainen, J. Laser overlap welding of Zn-coated steels on aluminium alloy for patchwork blank application in the automotive industry. *Rev. Adv. Mater. Sci.* **2015**, *40*, 295–302.
16. Akhter, R.; Steen, W.M.; Watkins, K.G. Welding Zinc-Coated Steel with a Laser and the Properties of the Weldment. *J. Laser Appl.* **1991**, *3*, 9–20. [CrossRef]
17. Zdravecká, E.; Slota, J. Mechanical and Microstructural Investigations of the Laser Welding of Different Zinc-Coated Steels. *Metals* **2019**, *9*, 91. [CrossRef]
18. Zhang, Z.; Zhao, Y.; Wu, S.; Lu, H. Optimization of Butt Welding of Zinc-Coated Thin Sheets with Oscillating Fiber Laser Beams: Weld Formation, Microstructure, and Mechanical Properties. *Weld. World* **2021**, *65*, 1711–1723. [CrossRef]
19. Akhter, R.; Group, J.P. Laser Welding of Zinc Coated Steel. Ph.D. Thesis, Imperial College London, London, UK, July 1990.
20. Bleck, W.; Guo, X.; Ma, Y. The TRIP Effect and Its Application in Cold Formable Sheet Steels. *Steel Res. Int.* **2017**, *88*, 1700218. [CrossRef]
21. *JIS G3302*; Hot-Dip Zinc-Coated Steel Sheet and Strip. Japanese Industrial Standards Committee: Tokyo, Japan, 2019.
22. *EN ISO 17637*; Non-Destructive Testing of Welds—Visual Testing of Fusion-Welded Joints. ISO: Geneva, Switzerland, 2017.
23. *ASTM E837-20*; Standard Test Method for Determining Residual Stresses by the Hole-Drilling Strain-Gage Method. ASTM International: West Conshohocken, PA, USA, 2020.
24. *SRPS EN ISO 15614-1:2017*; Specification and Qualification of Welding Procedures for Metallic Materials-Welding Procedure Test-Part 1: Arc and Gas Welding of Steels and Arc Welding of Nickel and Nickel Alloys-Amendment 1 (ISO 15614-1:2017/Amd 1:2019). ISO: Geneva, Switzerland, 2017.
25. *SRPS EN ISO 4136:2022*; Destructive Tests on Welds in Metallic Materials-Transverse Tensile Test (ISO 4136:2022). ISO: Geneva, Switzerland, 2022.
26. *SRPS EN ISO 6892-1:2020*; Metallic Materials-Tensile Testing-Part 1: Method of Test at Room Temperature (ISO 6892-1:2019). ISO: Geneva, Switzerland, 2020.
27. *SRPS EN ISO 9015-2:2017*; Destructive Tests on Welds in Metallic Materials-Hardness Testing-Part 2: Microhardness Testing of Welded Joints (ISO 9015-2:2016). ISO: Geneva, Switzerland, 2017.
28. *SRPS EN ISO 6507-1:2023*; Metallic Materials-Vickers Hardness Test-Part 1: Test Method (ISO 6507-1:2023). ISO: Geneva, Switzerland, 2023.
29. *SRPS EN ISO 9227:2023*; Corrosion Tests in Artificial Atmospheres-Salt Spray Tests (ISO 9227:2022). ISO: Geneva, Switzerland, 2022.

30. *SRPS EN ISO 5817:2023*; Welding-Fusion-Welded Joints in Steel, Nickel, Titanium and Their Alloys (Beam Welding Excluded)-Quality Levels for Imperfections (ISO 5817:2023). ISO: Geneva, Switzerland, 2023.
31. Maksymova, S.V.; Zvolinskyy, I.V.; Yurkiv, V.V.; Minakov, S.M.; Lysak, V.V. Residual Stresses in Thin-Sheet Galvanized Steel Joints after Arc Welding and Plasma Brazing. *Paton Weld. J.* **2020**, *2020*, 31–35. [CrossRef]
32. Silva, C.C.; De Assis, J.T.; Philippov, S.; Farias, J.P. Residual Stress, Microstructure and Hardness of Thin-Walled Low-Carbon Steel Pipes Welded Manually. *Mater. Res.* **2016**, *19*, 1215–1225. [CrossRef]
33. Zieliński, A.; Golański, G.; Sroka, M. Comparing the Methods in Determining Residual Life on the Basis of Creep Tests of Low-Alloy Cr-Mo-V Cast Steels Operated beyond the Design Service Life. *Int. J. Press. Vessel. Pip.* **2017**, *152*, 1–6. [CrossRef]
34. Petreski, M.; Runchev, D.; Vrtanoski, G.; Zdraveski, F.; Stankoski, M. Effect of laser beam and arc power on weld beam geometry in hybrid laser arc welding of structural steel. *Weld. Welded Struct.* **2024**, *69*, 157–163. [CrossRef]
35. Petreski, M.; Runchev, D.; Vrtanoski, G. Impact analysis of the hybrid laser arc welding parameters of structural steels: State of the art. *Weld. Welded Struct.* **2023**, *68*, 157–167. [CrossRef]
36. Cuddy, L.J.; Lally, J.S.; Porter, L.F. Improvement of Toughness in the HSLA of High Heat Input Welds in Ship Steels. In *Proceedings of the HSLA Steels Technology and Application*; Korchynsky, M., Ed.; American Society for Metals: Pittsburgh, PA, USA, 1984; p. 697.
37. Pereloma, E.; Edmonds, D. *V Phase Transformations in Steels*, 1st ed.; Woodhead Publishing: Sawston, UK, 2012; Volume 1.
38. Kirkaldy, J.S. Prediction of Microstructure and Hardenability in Low Alloy Steels. In *Proceedings of the International Conference on Phase Transformation in Ferrous Alloys*; AIME: Warrendale, PA, USA, 1983; pp. 125–148.
39. Manoharan, K.; Quazi, M.M.; Bashir, M.N.; Salleh, M.N.M.; Zafiuddin, A.Q.; Linggamm, R. An Overview of Laser Welding of High Strength Steels for Automotive Application. *Int. J. Technol. Eng. Stud.* **2020**, *6*, 23–40. [CrossRef]
40. Dasgupta, A.K.; Mazumder, J. Laser Welding of Zinc Coated Steel: An Alternative to Resistance Spot Welding. *Sci. Technol. Weld. Join.* **2008**, *13*, 289–293. [CrossRef]
41. Mei, L.; Chen, G.; Jin, X.; Zhang, Y.; Wu, Q. Research on Laser Welding of High-Strength Galvanized Automobile Steel Sheets. *Opt. Lasers Eng.* **2009**, *47*, 1117–1124. [CrossRef]
42. Wang, H.; Duan, Y.; Hao, S.; Guan, Y. Effect of Laser Welding on Performance of the B1500HS/340LA High-Strength Steel. *Metals* **2025**, *15*, 393. [CrossRef]
43. Zhou, S.; Zhao, Y.; Peng, Z.; Ren, F. The Investigation of Laser Lap Welding Process on High-Strength Galvanized Steel Sheets. *ISRN Mech. Eng.* **2011**, *2011*, 1–7. [CrossRef]
44. Kam, D.H.; Lee, T.H.; Kim, D.Y.; Kim, J.; Kang, M. Weld Quality Improvement and Porosity Reduction Mechanism of Zinc Coated Steel Using Tandem Gas Metal Arc Welding (GMAW). *J. Mater. Process. Technol.* **2021**, *294*, 117127. [CrossRef]
45. Dikić, S.; Glišić, D.; Fadel, A.; Jovanović, G.; Radović, N. Structure and Strength of Isothermally Heat-Treated Medium Carbon Ti-V Microalloyed Steel. *Metals* **2021**, *11*, 1011. [CrossRef]
46. Volovitch, P.; Allely, C.; Ogle, K. Understanding Corrosion via Corrosion Product Characterization: I. Case Study of the Role of Mg Alloying in Zn–Mg Coating on Steel. *Corros. Sci.* **2009**, *51*, 1251–1262. [CrossRef]
47. Volovitch, P.; Vu, T.N.; Allély, C.; Abdel Aal, A.; Ogle, K. Understanding Corrosion via Corrosion Product Characterization: II. Role of Alloying Elements in Improving the Corrosion Resistance of Zn–Al–Mg Coatings on Steel. *Corros. Sci.* **2011**, *53*, 2437–2445. [CrossRef]
48. Peng, W.; Duan, T.; Hou, J.; Guo, X.; Zhang, Y.; Ma, L.; Yu, M.; Xin, Y.; Xing, S.; Zhang, H. Electrochemical Corrosion Behavior of High Strength Steel in Simulated Deep-Sea Environment under Different Hydrostatic Pressure. *J. Mater. Res. Technol.* **2023**, *23*, 2301–2316. [CrossRef]
49. Malla, A.D.; Williams, G.; Britton, D.A.; Goodwin, F.E.; Cardoso, A.P.D.; Richards, T.; Penney, D.J.; Sullivan, J.H. Influence of Mg and Al Alloying Additions on the Corrosion Mechanisms of Hot-Dipped Zn-Mg-Al Coatings: Role of Microstructure and Phase Distribution. *npj Mater. Degrad.* **2025**, *9*, 96. [CrossRef]

Disclaimer/Publisher's Note: The statements, opinions and data contained in all publications are solely those of the individual author(s) and contributor(s) and not of MDPI and/or the editor(s). MDPI and/or the editor(s) disclaim responsibility for any injury to people or property resulting from any ideas, methods, instructions or products referred to in the content.